Structural phase transitions in the geometric ferroelectric LaTaO$_4$

Grant W. Howieson [ORCID],[1] Karuna K. Mishra,[2] Alexandra S. Gibbs [ORCID],[3] Ram S. Katiyar,[2] James F. Scott,[1,4]
Finlay D. Morrison [ORCID],[1,*] and Michael Carpenter[5,*]

[1]*EaStCHEM, School of Chemistry, University of St Andrews, St Andrews, KY16 9ST, United Kingdom*
[2]*Department of Physics and Institute for Functional Nanomaterials, University of Puerto Rico, San Juan, PR, 00931-3334, USA*
[3]*ISIS Facility, Rutherford Appleton Laboratory, Chilton, Oxon, OX11 0QX, United Kingdom*
[4]*SUPA, School of Physics and Astronomy, University of St Andrews, St Andrews, KY16 9SS, United Kingdom*
[5]*Department of Earth Sciences, University of Cambridge, Cambridge, CB2 3EQ, United Kingdom*

The recent report of an intermediate incommensurately modulated orthorhombic phase in LaTaO$_4$ has prompted a re-examination of the phase transition sequence in LaTaO$_4$ as a function of temperature. With falling temperature, the sequence of phases examined is (orthorhombic) $Cmc2_1$(C) $\leftrightarrow$ $Cmc2_1$(IC) $\leftrightarrow$ (monoclinic)$P2_1/c$, with C and IC denoting commensurate and incommensurate phases, respectively. The orthorhombic to monoclinic transition, T_{m-o}, is a first order reconstructive transition occurring at 440 K and T_{IC-C} is a first-order displacive transition occurring at 500–530 K. Strain and elasticity data confirm a first-order transition between the basic and modulated $Cmc2_1$ phases, with similarities to the isostructural fluoride BaMnF$_4$. A Raman spectroscopic study of the LaTaO$_4$ phase transition indicates that the IC-C phase transition is driven by a soft zone-boundary phonon (unstable) of the commensurate orthorhombic ($Cmc2_1$) phase. The soft phonon is found to appear (underdamped) above 443 K and vanishes (overdamped) around 528 K. A large supercell of the monoclinic phase below T_{m-o} is proposed based on the Raman spectroscopic results.

I. INTRODUCTION

LaTaO$_4$ is an $n = 2$ member of the series $A_nB_nX_{3n+2}$. This family of materials, which is becoming more popularly regarded as the Carpy-Galy phases [1,2], has been widely studied and bear similarities to the Dion-Jacobson and Ruddlesden-Popper structures. These materials have a stoichiometric excess of anions which induce separations in the three-dimensional connectivity of the octahedra in the {110} plane. The $A_nB_nX_{3n+2}$ series are known as the [110] phases due to this fact and their members can then be thought of as being comprised of sheets of corner-sharing octahedra stacked perpendicular to the {110} plane. These sheets are n octahedra thick and hence n indicates the anisotropy of the material; lower values indicate more quasi-two-dimensional structures, and the three-dimensional cubic perovskite structure is approached as n increases. Several ferroelectric materials adopt this structure type and the $n = 4$ oxides La$_2$Ti$_2$O$_7$ and Sr$_2$Nb$_2$O$_7$ are the most studied. They have an incommensurate ($Cmc2_1$) orthorhombic phase with a periodic modulation orthogonal to the polar axis [3,4]. The $n = 2$ fluorides, BaMF$_4$ (M = Mg, Fe, Ni, Zn, Mn), which are isostructural with LaTaO$_4$, have also been investigated for their ferroelectric properties, with all but Mn and Fe phases being shown to switch under an applied field [5,6]. BaMnF$_4$ has also been shown to exhibit an incommensurate-commensurate transition

at ~250 K between two $A2_1am$ (alternate setting of $Cmc2_1$) phases [7]. However, in contrast to the $n = 4$ oxides, the incommensurate modulation in BaMnF$_4$ lies along the polar axis.

LaTaO$_4$ is the only $n = 2$ ferroelectric oxide reported to date and its basic structural properties have been well established [8–12]. Mode analysis of the $Cmc2_1$ phase shows the presence of two gamma modes, Γ_1^+ and Γ_2^-, with reference to the parent $Cmcm$ structure. Since this transition only consists of zone-center gamma modes, the orthorhombic phase of LaTaO$_4$ is a proper ferroelectric. For the monoclinic $P2_1/c$ phase, three modes are observed, Γ_1^+, Γ_2^+ and S_2^-, which introduces antiphase tilting of the octahedra and accompanying alternating displacement of the La cations (making this phase essentially anti-polar). The structure of these phases relative to the parent aristotype is shown in Fig. 1. A first-principles investigation of LaTaO$_4$ has noted the parent structure and monoclinic phase are only separated by a very small energy barrier (0.26 meV per formula unit), and a similarly small barrier exists between the monoclinic and orthorhombic phases (58 meV per formula unit), making the $Cmc2_1$ phase metastable [13].

The parent $Cmcm$ phase has yet to be accessed experimentally but it is expected that on cooling from this phase, LaTaO$_4$ directly transforms to the metastable ferroelectric $Cmc2_1$ phase, before developing an incommensurately modulated $Cmc2_1$ phase on further cooling (discussed below). At lower temperatures, LaTaO$_4$ will then transform into its stable anti-polar $P2_1/c$ structure. Although each of these phases are subgroups of the $Cmcm$ parent, $Cmc2_1$ and $P2_1/c$ structures

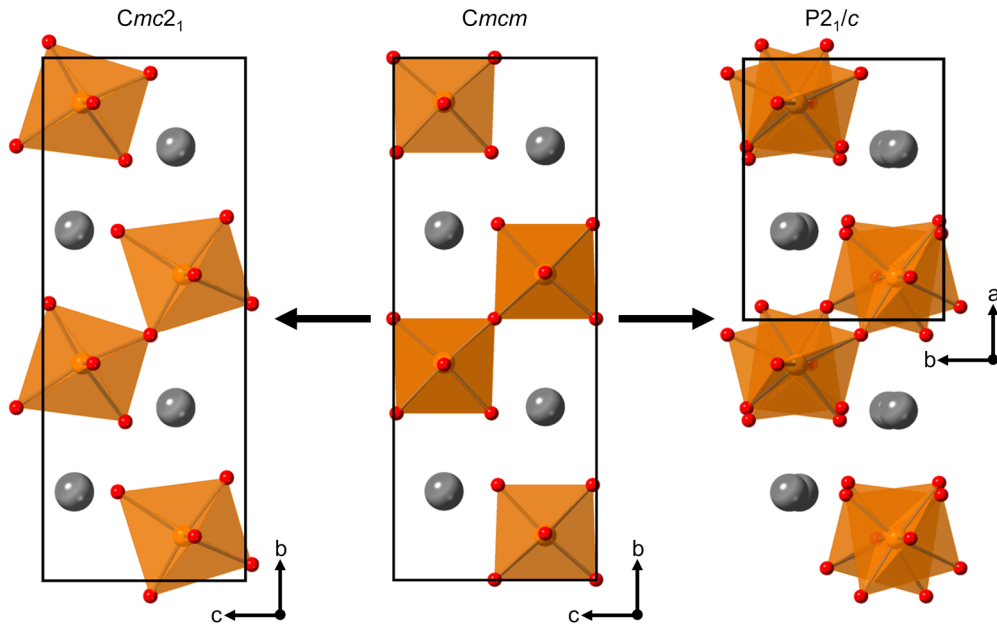*Corresponding authors: finlay.morrison@st-andrews.ac.uk; mc43@esc.cam.ac.uk

FIG. 1. Structure of the parent *Cmcm* phase (middle) with the orthorhombic *Cmc*2_1 (left) and monoclinic *P*$2_1/c$ (right) subgroups. Grey, orange, and red spheres represent La, Ta and O atoms, respectively.

are not subgroups of each other, and the transition between them is necessarily first order.

LaTaO$_4$ may adopt the polar orthorhombic *Cmc*2_1 or nonpolar monoclinic *P*$2_1/c$ phase at ambient conditions as determined by the synthesis temperature and also according to whether samples are sintered as loose powders or pellets; higher temperatures and preparation as pellets give rise to higher monoclinic content [8–10]. Vullum *et al.* [9] observed that mixed orthorhombic/monoclinic samples transform to monoclinic under an applied pressure of 150–170 MPa at ambient conditions. In addition to externally applied stress or stresses induced during synthesis in pellet form, chemical pressure due to doping with smaller lanthanoids such as Nd also stabilizes the monoclinic phase [11]. The monoclinic phase also transforms to the orthorhombic phase on heating as described in detail below. All of these observations are consistent with the relatively lower molar volume of the monoclinic LaTaO$_4$ phase (326.15 Å^3 at 293 K compared to 327.07 Å^3 for the orthorhombic phase) and the positive temperature vs pressure relationship according to the Clausius–Clapeyron equation [9].

Samples synthesized in this investigation, which are monoclinic (*P*$2_1/c$) at ambient conditions, undergo a first-order structural transition to the orthorhombic (*Cmc*2_1) phase at ~440 K on heating but display a significant thermal hysteresis, transforming back to monoclinic at ~300 K. Transitions between the *P*$2_1/c$ and *Cmc*2_1 phases are easily detected by means of dielectric spectroscopy, but this technique also reveals a second dielectric anomaly at approximately 500 K (this feature exhibits little thermal hysteresis) and is also present in samples that are already stabilized in the *Cmc*2_1 phase at ambient [11,12]. Until recently, the origin of this dielectric anomaly was subject to debate, but we have identified it as an incommensurate [*Cmc*$2_1(\alpha00)0s0$] to commensurate (*Cmc*2_1), IC-C transition [14]. The modulation of this phase was found to arise as a partial ordering of smaller subunits

in the *a* axis, which led to an overall modulation wave vector of $q = (0.456, 0, 0)$ at 483 K (active irrep $\Sigma_2[0.456, 0, 0]$). Since the structure is only modulated in the *a* axis the wave vector only contains an *a** component, which is found to be negatively correlated with temperature. This means that modulation increases in length with increasing temperature in real space, i.e., from an average repeat of 2.179 *a* at 323 K to 2.193 *a* at 483 K. The increasing length of the real-space modulation is thought to be due to an increased ordering of these subunits as a function of temperature [14]. The existence of these smaller subunits, which are 3 × and 2.5 × expansions of the basic cell in the *a* axis, was hypothesized to be the result of a mechanism that rectifies an irregular La bonding environment, as seen in $n = 4$ phases [3].

In light of this incommensurately modulated intermediate phase, the present study aims to re-explore the overall structural evolution of LaTaO$_4$ samples synthesized to be stable as either monoclinic or orthorhombic at ambient conditions.

II. EXPERIMENTAL

All reagents (>99% purity) were dried for 1 h prior to use: La$_2$O$_3$ at 1273 K and Ta$_2$O$_5$ at 873 K. Stoichiometric amounts of the oxides were mixed by milling at 600 rpm for one hour in a planetary ball mill and pressed into 10–13 mm diameter pellets either under 1 ton uniaxial load or 200 MPa of isostatic pressure. Pellets were then annealed at temperatures between 1623 and 1923 K for 6 h. Synthetic conditions were selected in order to stabilize either the monoclinic or orthorhombic phase at room temperature: Sample A (highest *o*-LaTaO$_4$ content at ambient conditions) was produced by uniaxial pressing and annealing at 1623 K, whereas Sample B (highest *m*-LaTaO$_4$ content) was produced by annealing under the harsher conditions of isostatic pressing and annealing at 1923 K.

Powder x-ray diffraction (PXRD) was used to confirm the structure of samples at ambient temperature. Variable

temperature powder neutron diffraction (PND) data for Sample A was also collected using the high-resolution powder diffractometer (HRPD) at ISIS as described in Ref. [14]. Samples were first heated to above 523 K to transform any residual monoclinic phase to orthorhombic and data were subsequently collected on cooling from 523 K at 2 K increments to 483 K; for close observation of the IC-C phase transition; collection time for each time was 1 h (40 μAh integrated proton current to the target), except 483 and 523 K, which was 3 h (120 μAh). Data were also collected between 473 and 323 K at 50 K increments for observation of the modulation vector as a function of temperature, all collection times were 3 h (120 μAh). Sample B contained minimal orthorhombic impurity at ambient conditions ($<1\%$). Approximately 5 g of sample was analyzed. Data points between 300 and 500 K are from a previous study by Cordrey *et al.* [11]. These were also collected using the HRPD facility, with a collection time of $\sim$40 min ($\sim$30 μAh) per data point. PXRD was used to determine the Sample B lattice parameters and was conducted using a PANalytical Empyrean Cu x-ray tube diffractometer with a primary beam monochromator (CuKa1) and X'celerator RTMS detector. PXRD data were refined by the Rietveld method using GSAS software [15,16], with Jana2006 [17] being implemented in refining the incommensurate structure from PND data. Details of refinements and final tabulated parameters are given in the Supplemental Material [18].

Details of the resonant ultrasound spectroscopy (RUS) technique are described fully in the literature (see Migliori and Sarrao, for example) [19]. For the experiments described here, polycrystalline pellets of each sample were cut into rectangular parallelepipeds and the piece with the best RUS signal, i.e., giving the clearest resonance peaks, was selected for high temperature measurements. Sample A had dimensions 2.731 $\times$ 1.656 $\times$ 1.215 mm^3 and mass 0.0269 g. Sample B had dimensions 2.239 $\times$ 1.965 $\times$ 1.349 mm^3 and mass 0.0416 g. The parallelepipeds were placed across a pair of corners between the tips of alumina buffer rods inside a horizontal Netzsch furnace, as described in Ref. [20]. In this set up, piezoelectric transducers are attached to the ends of the buffer rods, outside the furnace, one to provide the exciting signal and the other to detect resonances of the sample and rods. Data were collected in successive heating and cooling cycles; a detailed description of temperature ranges and increments are given in the Supplemental Material [18].

Raman spectra were measured employing a HORIBA Jobin Yvon micro-Raman spectrometer (model: T64000) equipped with a 50 X long-working distance objective lens. The experiments were carried out in backscattering geometry (180°) using a 514.5-nm line of an Ar$^+$ ion laser (Coherent, Innova 70-C). Temperature dependent Raman spectra were recorded from 298 to 583 K in a close temperature interval using a Linkam heating/cooling stage ensuring temperature stability of $\pm$ 0.1 K. The signal-to-noise ratio was improvised by adjusting laser power and acquisition time to obtain better Raman spectra. The scattered signals from the sample were analyzed using a triple monochromator and detected by a liquid nitrogen cooled CCD detector. The spectrometer resolution for 1800 lines/mm grating was about 1 cm^{-1}. The Raman spectra were analyzed using Lorentzian line

shapes to obtain the band frequencies, linewidths, and their intensities.

III. RESULTS

A. Structural evolution with temperature

The parent (aristotype) structure of LaTaO$_4$ is taken to be in space group $Cmcm$, which is nonpolar. There are two derivative structures which develop from this by different combinations of octahedral tilting as described previously and are shown in Fig. 1: (a) An orthorhombic structure with space group $Cmc2_1$, which is polar and has the same unit cell dimensions as the parent $Cmcm$ structure (but with an incommensurate repeat of $\sim$2.2 unit cells along the a axis, as identified in our previous study [14]), and (b) a monoclinic structure with space group $P2_1/c$, which is nonpolar. As mentioned above, synthesis conditions can be adjusted to predetermine which LaTaO$_4$ polymorph will be stabilized at ambient conditions.

Initial PXRD analysis of each sample allowed data from Sample A and Sample B to be fitted primarily in $Cmc2_1$ and $P2_1/c$ space groups, respectively, but with evidence for the presence of small amounts of the other polymorph. Rietveld refinement of the PND data at 323 K allowed a more accurate determination of the phase fractions to be established, with Sample A initially containing $\sim$10 wt% monoclinic phase and Sample B containing <1 wt. % orthorhombic phase. Given the large thermal hysteresis associated with the $P2_1/c \leftrightarrow Cmc2_1$ (IC) transition, measurements on Sample A were collected during cooling after first heating to transform any monoclinic phase and therefore mitigate against the need for a two-phase refinement.

As the IC-C transition is approached on cooling, clear emergence of the second low temperature incommensurate $Cmc2_1$ phase is observed. The data in this region of phase coexistence is therefore fitted to a mixture of low (IC) and high (C) temperature $Cmc2_1$ phases each with distinct lattice parameters. The IC phase is slightly contracted in the a-c plane but with a much larger b axis as a result the modulation inhibiting the close packing of the octahedral sheets compared to that of the commensurate $Cmc2_1$ phase [14]. The satellite peaks associated with the IC phase are only detectable by PND and disappear with increasing temperature.

As mentioned previously, dielectric spectroscopy provides a simple method for identification of the phase transition sequence and Fig. 2 shows data for relative permittivity as a function of temperature for both samples. This permittivity data is consistent with previous investigations [11,12]: Sample A shows one dielectric anomaly at $\sim$485 K associated with the $Cmc2_1$(C) $\leftrightarrow Cmc2_1$(IC) transition, with a small amount ($\sim$5 K) of thermal hysteresis. Sample B shows an anomaly associated with a transition between the $P2_1/c$ and $Cmc2_1$ (IC) phases at $\sim$430 K, with a large thermal hysteresis (>170 K). Dielectric data for Sample B also contains the anomaly associated with the IC-C transition but occurring 10–20 K higher than in Sample A.

The sequence with decreasing temperature on cooling to ambient in Sample A is $Cmc2_1$(C) $\rightarrow Cmc2_1$(IC). The
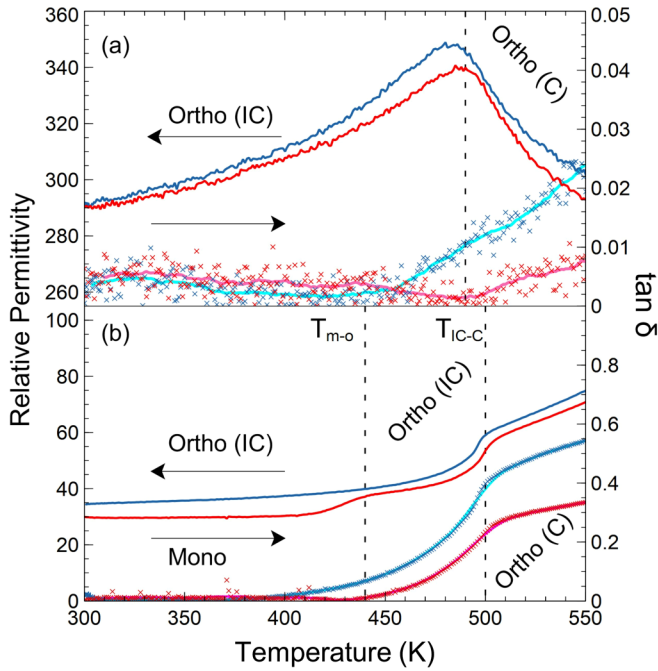
FIG. 2. Dielectric data (at 400 kHz) as a function of temperature for: (a) Sample A (b) Sample B. The anomaly attributed to a $Cmc2_1$(C) $\rightarrow$ $Cmc2_1$(IC) transition in the data for Sample A occurs at ~488 K during heating and ~483 K during cooling. The related maximum in relative permittivity for Sample B occurs at ~501 K during heating and ~496 K during cooling. The anomaly in the Sample B data at ~430 K (heating) is attributed to the $P2_1/c \rightarrow Cmc2_1$ (IC) transition. Due to the noise in the loss data (tan δ) for Sample A a 21-point moving average is included to guide the eye.

sequence with falling temperature in Sample B is $Cmc2_1$(C) $\rightarrow$ $Cmc2_1$(IC) $\rightarrow$ $P2_1/c$. At some high temperature both would be expected to eventually transform to the parent (untilted) $Cmcm$ structure. $Cmc2_1$ and $P2_1/c$ are different subgroups of $Cmcm$; the active representation for $Cmcm \rightarrow Cmc2_1$ is Γ_2^- [13]; the order parameter has one component and the $Cmc2_1$ phase is a proper ferroelectric. This transition is allowed by symmetry to be thermodynamically continuous. The $Cmc2_1$(C) $\rightarrow$ $Cmc2_1$(IC) transition is likewise allowed by symmetry to be thermodynamically continuous and it is commonly found that transitions to incommensurate structures are second order in character. $P2_1/c$ is a subgroup of $Cmcm$ but not of $Cmc2_1$ (including the IC structure), so that $Cmc2_1$(IC) $\rightarrow$ $P2_1/c$ is necessarily first order; the order parameter has one nonzero component and the transition is improper ferroelectric.

B. Strain analysis

Experimental data for the variations in lattice parameters as a function of temperature were obtained up to 773 K in a cooling sequence for Sample A and in both heating and cooling sequences up to 573 K for Sample B. These are reproduced in Fig. 3. Sample A exists in the incommensurate orthorhombic $Cmc2_1(\alpha00)0s0$ phase in the range of ~300–500 K, where there is positive thermal expansion (PTE) in the a and c axes and negative thermal expansion (NTE) of the b axis. Sample A

then transitions to the unmodulated phase at ~500 K, which is marked by a clear decrease in the (positive) thermal expansion coefficient of a and c and change to PTE in the b axis. Sample B, which exists in the monoclinic phase under ambient conditions, shows PTE of all axes until it transitions to the incommensurate orthorhombic phase at ~440 K. Once in the IC phase, the lattice parameters exhibit the same behavior as with Sample A, namely PTE in a and c with NTE in b until the IC-C transition at ~440 K above which it exhibits PTE in all axes.

The uniaxial NTE exhibited by the IC orthorhombic phase is common in layered perovskites and is generally attributed to condensation of octahedral rotation modes and anisotropic elastic compliance [21]. In our current investigation, it is important to note that uniaxial NTE is only observed in incommensurate $Cmc2_1(\alpha00)0s0$ phase and reverts to PTE at the IC-C transition. This strongly suggests that the NTE behavior in this case is driven by the incommensurate octahedral tilting which inhibits effective packing of the perovskite layers along the b axis [14]. Ablitt *et al.* showed that for LaTaO$_4$ the Γ_1^+ mode, which contributes to the octahedral tilting, means that the rotation angles of the octahedra respond to changes in the c axis [21]. It is therefore likely that the metastable IC phase arises to alleviate strain in the c axis; this is consistent with our observation that Nd-doping stabilizes the IC phase as a result of chemical pressure [14].

Variations of the spontaneous strain components e_1, e_2, and e_3 which develop below the $Cmc2_1$(C) $\rightarrow$ $Cmc2_1$(IC) transition in Sample A (o-LaTaO$_4$ at ambient) have been determined by first fitting straight lines to data collected in the interval 573–773 K and extrapolating these to lower temperatures to give variations of the reference parameters a_o, b_o, c_o [Figs. 3(a)–3(c)]. Values of the three linear strains obtained from $e_1 = (a - a_o)/a_o$, $e_2 = (b - b_o)/b_o$, $e_3 = (c - c_o)/c_o$ are shown in Fig. 3(f). They have magnitudes up to ~1%, which is greater than the strains typically associated with octahedral tilting transitions in perovskites [such as (Ca, Sr)TiO$_3$, for example] [22]. It is interesting to note that the incommensuration introduces a negative c-axis strain (e_3) consistent with the description above. Each strain component shows the same pattern of nonlinear variation and what appears to be a steep drop in magnitude between 473 and 523 K.

The solution for a first-order transition from a 246 Landau expansion, as would apply in this case, is

$$q^2 = \frac{2}{3}q_o^2 \left\{ 1 + \left[1 - \frac{3}{4}\left(\frac{T - T_c}{T_{tr} - T_c} \right) \right]^{1/2} \right\}, \quad (1)$$

where q is the order parameter, q_o represents the magnitude of the discontinuity in q at the transition temperature, T_{tr}, and T_c is the critical temperature. Individual strains are related to q according to $e_1 \propto e_2 \propto e_3 \propto q^2$. Replacing q^2 by e and q_o^2 by e_o leads to the fits to e_2 and e_3 shown in Fig. 3(f), representing a weakly first-order transition with $T_{tr} \approx 510$ K. The overall pattern is clear, but the fit parameters are not tightly constrained because of the limited number of data points. A "best" fit has been obtained by combining the three linear strains as a scalar strain, $e_{scalar} = \sqrt{e_1^2 + e_2^2 + e_3^2}$, and the fit parameters for the curve shown in Fig. 3(f) are $T_c = 516$ K, $T_{tr} = 518$ K,
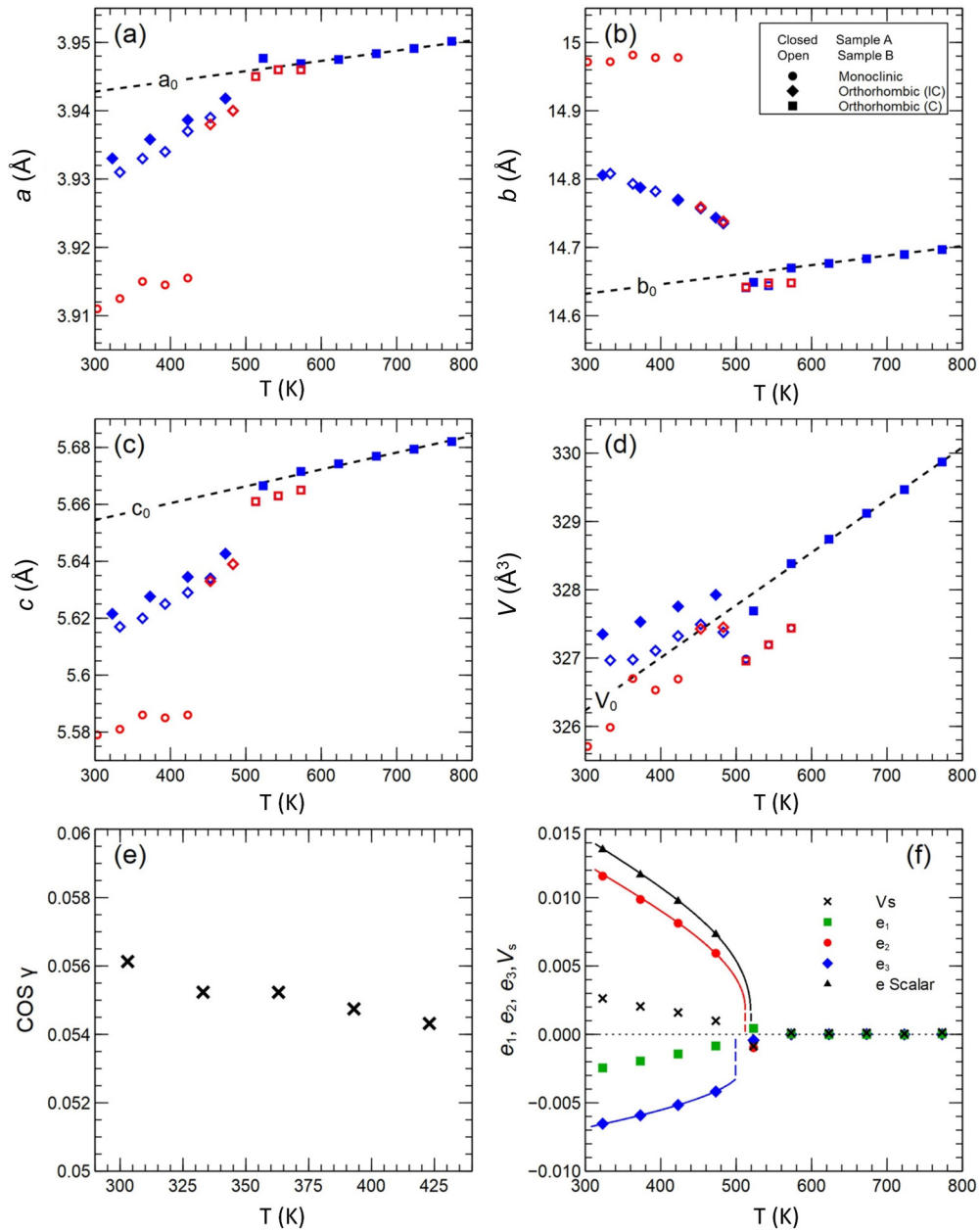
FIG. 3. Strain analysis based on lattice parameters. (a)–(d) Lattice parameters for both Sample A and B. Data for the $P2_1/c$ structure are expressed in terms of the unit cell of the $Cmc2_1$ structure. Linear variations of the reference parameters, a_o, b_o, c_o, V_o, for calculation of spontaneous strains were obtained by fitting to data of Sample A (initially o-LaTaO$_4$ at ambient) in the temperature interval 573–773 K. Variations of lattice parameters of Sample B (initially m-LaTaO$_4$ at ambient) are closely similar to those of Sample A. (e) Variation of $\cos\gamma (\approx e_6)$ for the monoclinic structure of Sample B, where γ is the monoclinic angle of a cell aligned with that of the $Cmc2_1$ structure. (f) Variation of spontaneous strains defined with respect to the $Cmc2_1$ structure of Sample A. Curves are fits of Eq. (1) to the data, consistent with the view that the $Cmc2_1 \rightarrow$ IC transition is weakly first-order and has a transition temperature, T_{tr}, between ∼510 and ∼520 K.

$e_o = 0.0016$. All three fits shown in Fig. 3(f) (curves, with discontinuities at T_{tr} shown as vertical dashed lines) have the same form, marking a weakly first-order transition at T_{tr} between ∼510 and ∼520 K with differences between T_{tr} and T_c of a few degrees. There is a small, positive volume strain ($V_s = (V - V_o)/V_o \leqslant \sim0.003$) associated with the transition when calculated in the same way as for the linear strains [Figs. 3(d) and 3(f)]. This is understood to be a consequence of the incommensuration; the modulated nature of the cation positions and associated octahedral tilting results in a small

contraction in the ac plane but imposes a larger effect in preventing close packing of octahedral sheets in b [14].

These lattice parameter variations are close to those reported for o-LaTaO$_4$ by Cordrey *et al.* [11], except for the values at 523 K. In that study the lattice parameters at 523 K seem to define a more nearly continuous transition with a slightly higher transition temperature. As part of the current study, a longer acquisition time for PND data at the IC-C transition allowed more well-defined diffraction peaks to be detected and this revealed clear phase coexistence of both the

high temperature (C) and low temperature (IC) phases. The seemingly continuous nature of the transition is symptomatic of a single phase refinement of unresolved (overlapping) peaks and hence the apparent continuous shift in parameters reported by Cordrey *et al.* [11]. Rietveld refinement of the data in this range requires multiple phases to be considered; one for the low temperature modulated structure and one for the basic high temperature structure. Only when the presence of both of these separate phases is considered can the parameters be correctly described [14].

Lattice parameters for the $Cmc2_1$ (C) and $Cmc2_1$ (IC) structures of Sample B do not quite overlap with those of Sample A but they show the same pattern of temperature dependence [Figs. 3(a)–3(e)]. The variations of e_1, e_2, e_3, and V_s would therefore also be closely similar and again suggest a weakly first-order transition with T_{tr} between 483 and 513 K.

The reference structure with $Cmcm$ symmetry needed for determination of spontaneous strains due to the $Cmcm \rightarrow Cmc2_1$ and $Cmcm \rightarrow P2_1/c$ transitions has not been observed. Comparison of the lattice parameter data is nevertheless revealing of differences in the strain variations. For this purpose, parameters of the $P2_1/c$ lattice have been recalculated to the same form of cell as for the $Cmc2_1$ structure. As an example, monoclinic cell parameters at 303 K, $a = 7.630$ Å, $b = 5.579$ Å, $c = 7.822$ Å, $\beta = 101.532°$, become $a = 3.911$ Å, $b = 14.972$ Å, $c = 5.579$ Å, $\gamma = 86.782°$. The parameters for this cell added to Figs. 3(a)–3(c) suggest that linear strains arising from the $Cmcm \rightarrow P2_1/c$ transition would be substantially greater than those arising from $Cmcm \rightarrow Cmc2_1$. On the other hand, the volume strains are likely to be quite similar, given that the differences in unit cell volume are relatively small [Fig. 3(d)]. The shear strain $e_6(\approx \cos\gamma)$ is strictly zero in the orthorhombic reference state and is therefore a true measure of spontaneous strain due to $Cmcm \rightarrow P2_1/c$. Observed values of nearly 6% [Fig. 3(e)] are consistent with the view that strains accompanying $Cmcm \rightarrow P2_1/c$ are large.

C. Elasticity

Figure 4 shows a stack of spectra collected in the second cooling sequence for Sample A. The *y* axis represents the amplified signal from the detecting transducer, in volts, but the spectra have been offset in proportion to the temperature at which they were collected (highest temperature at the top). Resonance peaks, which do not vary with temperature, are from the alumina buffer rods. Peaks which vary with temperature are from the sample and the one which can be followed most readily through most of the temperature range has a frequency of ∼345 kHz at 800 K. Blue peaks are fits to the data in the range where distinct elastic softening occurs with decreasing temperature.

Figure 5 contains the results of fitting the sample peak with frequency near 345 kHz at 800 K using an asymmetric Lorentzian function. Most resonances of a polycrystalline sample involve predominantly shearing motions with the consequence that the square of peak frequencies, f^2, can be taken to scale with the shear modulus. Q^{-1} is the inverse mechanical quality factor and is a measure of acoustic loss. In RUS measurements it is generally specified as $\Delta f/f$, where Δf is the
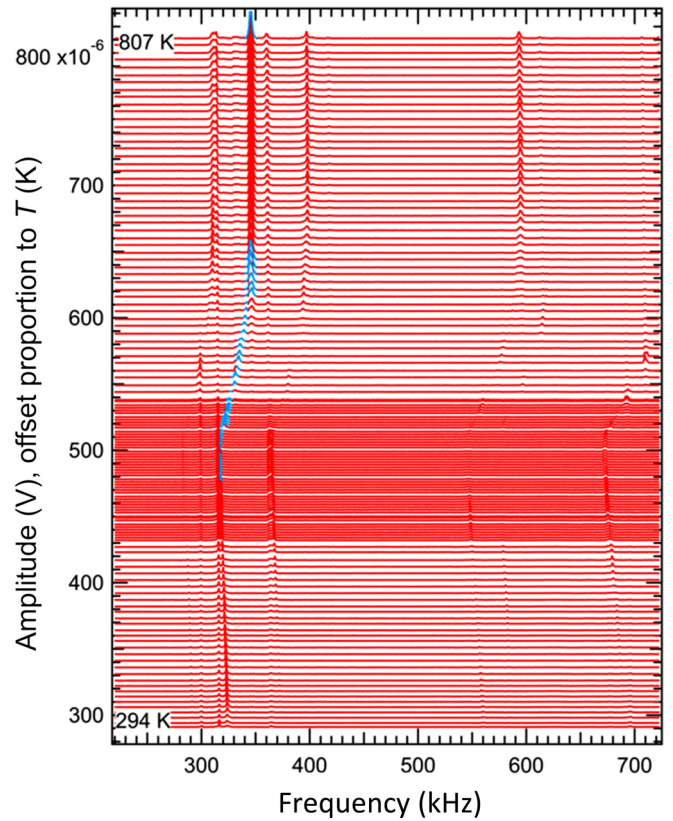

FIG. 4. Segments of RUS spectra from polycrystalline Sample A, collected in the second cooling sequence. They are stacked with offsets up the *y* axis in proportion to the temperature at which they were collected. Resonance peaks which do not change frequency with changing temperature are from the alumina buffer rods. Blue lines are fits to resonance peaks of the sample in the temperature interval of elastic softening with decreasing temperature.

peak width at half maximum height. Elastic softening starts below ∼650 K and has a rounded minimum at ∼510 K, before further slightly stiffening as temperature decreases further. The maximum softening amounts to ∼20% of the value at high temperatures. There are small differences between f^2 values between heating and cooling sequences in the temperature interval of softening and recovery. Q^{-1} is more or less constant from ∼800 K down to ∼480 K where it decreases to a more or less constant lower value. There is an increase in Q^{-1} with falling temperature below ∼310 K which appears to presage some increase in loss at lower temperatures.

By comparison with expected patterns of elastic softening for different types of phase transitions, as set out by Carpenter and Salje [23], the observed variation of f^2 is consistent with the $Cmc2_1$(C) → $Cmc2_1$(IC) transition being weakly first-order (consistent with PND analysis [14] and the Raman data described below), and having coupling between the driving order parameter and nonsymmetry breaking strains. The transition is coelastic, i.e., not involving any symmetry breaking strain, and the coupling terms for nonzero strains e_1, e_2, e_3 have the form λeq^2. Softening as the transition is approached from above can be accounted for by fluctuations, in the same manner as occurs ahead of the $\alpha - \beta$ transition in quartz [24]. Relatively low acoustic loss below the transition is consistent
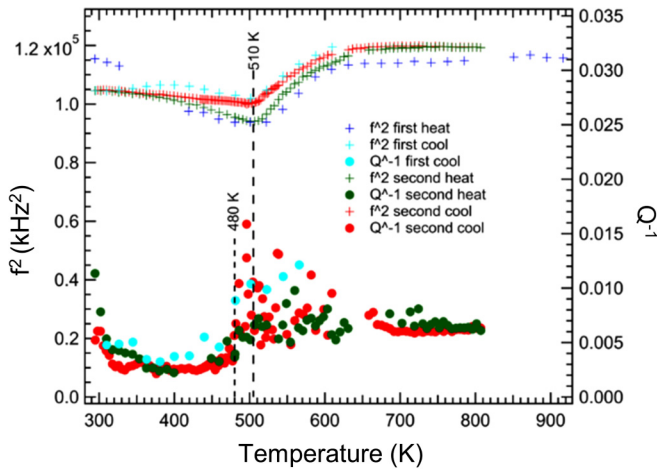
FIG. 5. Variations of f^2 and Q^{-1} from fitting of a single resonance peak in RUS spectra from a polycrystalline sample of Sample A, using an asymmetric Lorentzian function. The peak has frequency ∼345 kHz at 800 K. There is a rounded minimum in f^2 at ∼510 K and the small difference in values between heating and cooling has its maximum at the same temperature. There is a reduction in Q^{-1} at ∼480 K and the onset of an increase below ∼310 K. Scatter in the data for Q^{-1} between ∼500 and ∼600 K is, at least in part, an experimental artifact due to interaction of sample peaks with rod peaks.

with the absence of any microstructure, such as ferroelastic domain walls, that could be mobile under applied shear stress on a time scale of ∼10^{-6} s. Relatively high loss above the transition point implies that some aspect of the structure responds to externally applied dynamical stress. There is no real indication of a peak in Q^{-1} at the transition point which would be evidence of critical slowing down.

The RUS spectra for Sample B collected in the second cooling sequence are shown in Fig. 6 in the same format as for spectra from Sample A in Fig. 4. The resonance peaks in the spectra collected from this sample are clearly weaker than those obtained from Sample A. Most, if not all, of the resonance peaks in spectra collected below ∼440 K are from the buffer rods but the increased amplitude of these in frequency ranges which follow the temperature-dependent softening of sample peaks is due to interaction of buffer rod resonances with sample resonances that are too weak and/or broad to appear directly. There are several peaks which vary systematically with temperature at higher temperatures, however, and the peak which can be followed most readily through most of the temperature range has frequency ∼500 kHz at 800 K. Blue peaks are fits to this.

Variations of f^2 and Q^{-1} from fitting of the peak highlighted in Fig. 6 are shown as a function of temperature in Fig. 7, as well as variations for what appears to be the same peak in spectra collected in the prior experiments up to ∼1141 K. There are three main features. Firstly, f^2 (proportional to the shear modulus) shows a softening trend from 1141 K down to ∼580 K. There is then steep softening with decreasing temperature in the interval ∼580–520 K. This is followed by further softening down to room temperature. Secondly, resonance peaks from the sample are not directly
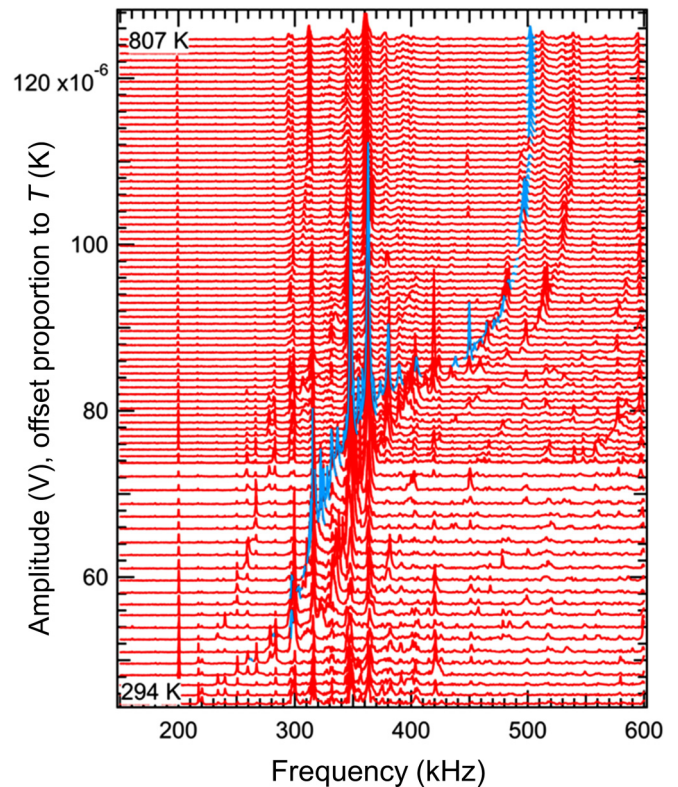

FIG. 6. Segments of RUS spectra from a polycrystalline sample of Sample B collected in the second cooling sequence. They are stacked with offsets up the y axis in proportion to the temperatures at which they were collected. Resonance peaks which do not change frequency with changing temperature are from the alumina buffer rods. Blue lines are fits to a resonance peak from the sample which has frequency ∼500 kHz at 800 K and appears to trend towards ∼220 kHz at room temperature.
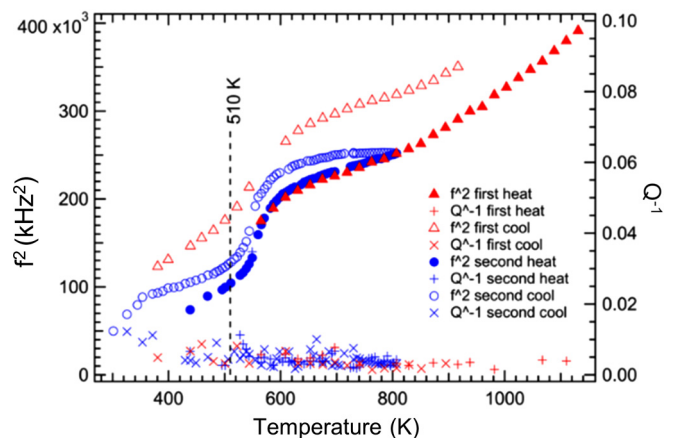

FIG. 7. Variations of f^2 and Q^{-1} from fitting of a resonance peak which has frequency ∼500 kHz at ∼800 K. Individual peaks from the sample became progressively weaker and harder to distinguish from buffer rod peaks below ∼430 K but the trend of elastic softening with falling temperature clearly continued below 350 K. A dashed line is shown at 510 K to mark the temperature at which a minimum in f^2 was seen in spectra from Sample A (Fig. 5).
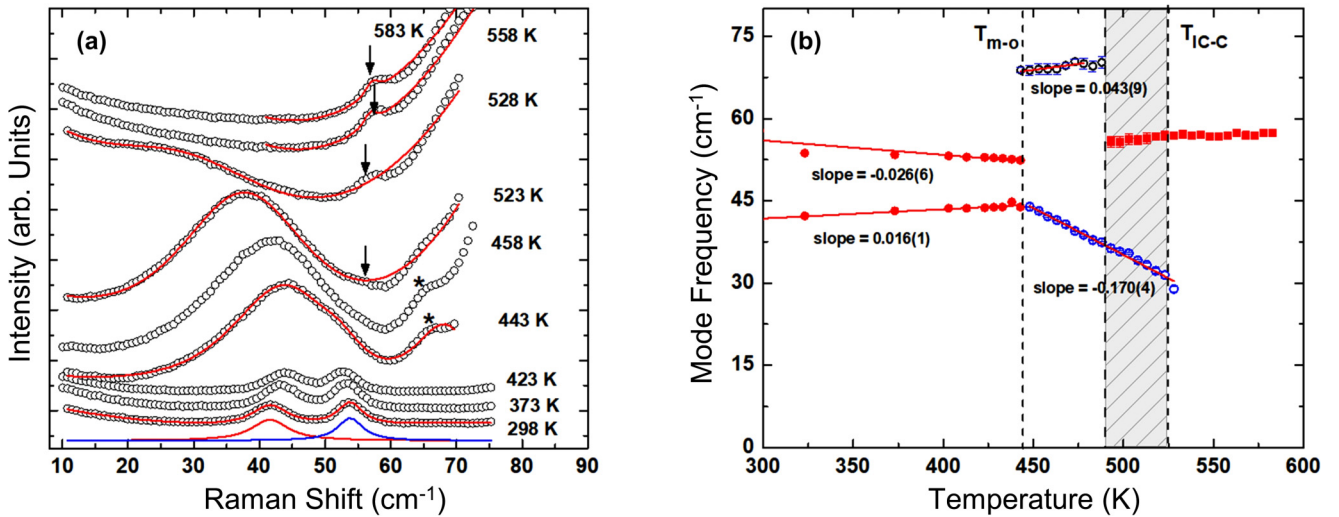
FIG. 8. Low frequency Raman data measured on Sample B on heating. (a) Raman spectra of m-LaTaO$_4$ sample measured at different temperatures from $T = 298$–583 K shows $T_{\text{m-o}}$ at ∼443 K and region of phase coexistence at associated with $T_{\text{IC-C}}$ at 493 - 528 K. Open circles are the experimental data. Continuous solid lines are fit for individual Raman bands and total Lorentzian fit to the data. The appearance of Raman modes are indicated by arrow and star symbols. (b) Temperature-dependent Raman mode frequencies of Sample B. Discontinuous changes of the mode frequencies are consistent with both transitions being first-order. A zone boundary soft mode of the $Cmc2_1$ (C) phase appears at $T_{\text{m-o}} = 443$ K with frequency 44 cm^{-1} and continuously softens, disappearing at ∼528 K.

visible in spectra collected below ∼400 K, indicating strong attenuation. Finally, there is a marked hysteresis between heating and cooling shown by f^2 variations in each of the two heating/cooling sequences. As for Sample A, f^2 values are higher during cooling than during heating but they show essentially the same overall pattern of temperature dependence. Holding the sample at ∼1141 K for 1–2 days resulted in a shift to higher frequencies of all the resonance frequencies. Data for Q^{-1} show scatter due to the fact that all resonances from this sample were weak, but they do not show any obvious features in the interval ∼1140–400 K.

The overall pattern of softening with decreasing temperature through the full temperature interval shown in Fig. 7 is very different from that shown by Sample A (Fig. 5). It amounts to a total softening by ∼80% over the full temperature interval in Fig. 7, rather than the ∼20% step seen in Fig. 5. Furthermore, although the spontaneous strain variations for the $Cmc2_1$(C) → $Cmc2_1$(IC) transition are almost indistinguishable for the two samples, the steep softening in the interval ∼580 to ∼520 K is larger than the softening in Sample A and shifted to higher temperatures. High acoustic loss below ∼440 K is consistent with the transition to a monoclinic structure because newly generated ferroelastic twin walls are likely to be mobile in response to an external stress in the same manner as seen in perovskites [25].

D. Raman spectroscopy

Observations of low frequency phonons(s) in fluorides such as BaMF$_4$ [7,26] (which is isostructural with LaTaO$_4$) are often associated with IC to C phase transitions. Low frequency Raman spectroscopy studies on such phonon modes in LaTaO$_4$ have not yet been reported. Therefore, it is of interest to examine the low energy phonon behavior on LaTaO$_4$ (Sample B) employing Raman spectroscopy to cover all the sequences of phase transitions of interest. Figure 8(a) shows the Raman spectra measured at various temperatures during a heating cycle. At room temperature (298 K) two Raman modes were identified in the frequency range 10–75 cm^{-1}. The spectra exhibit dramatic changes across the monoclinic $(P2_1/c) \leftrightarrow Cmc2_1$(IC) $\leftrightarrow Cmc2_1$(C) phase transition(s) from 298 to 583 K. Sudden changes in spectral features across the phase transition(s) indicate involvement of first-order transition(s). The two modes located at 42 and 54 cm^{-1} gradually shift towards each other during heating and then disappear at 443 K. A Raman mode at 67 cm^{-1} and another at 44 cm^{-1} begin to appear at 443 K. The band frequency of 44 cm^{-1} mode shifted downward with increasing temperature and can be attributed to a soft phonon as its frequency decreases linearly and vanishes as the temperature approaches 528 K, the temperature at which the last of the IC phase transforms. A discussion of the soft phonon is presented later.

As can be seen in Fig. 8(a), another new mode at 56 cm^{-1} begins to appear at 493 K and its intensity increases monotonically between 493 and 583 K. These spectral features of disappearance and appearance of phonon modes clearly corroborates the phase transition from low temperature monoclinic to $Cmc2_1$ (IC) phases at 443 K and $Cmc2_1$ (IC) to $Cmc2_1$ (C) between 493 and 528 K. By analogy with the intensities of superlattice reflection peaks in neutron powder diffraction patterns, examination of the intensities of Raman bands can help with the determination of phase fractions in regions of coexistence [27]. Coexistence of IC and C phases between 493 and 583 K is evident from the observation of a unique band at 56 cm^{-1} of the high temperature $Cmc2_1$ (C) phase as shown in Fig. 8(a). The intensity of this band increases with increasing temperature in the range 493–583 K. It suggests an increase in phase fraction of $Cmc2_1$ (C) phase and corroborates the coexistence of IC and C phases, in agreement with the neutron diffraction data.
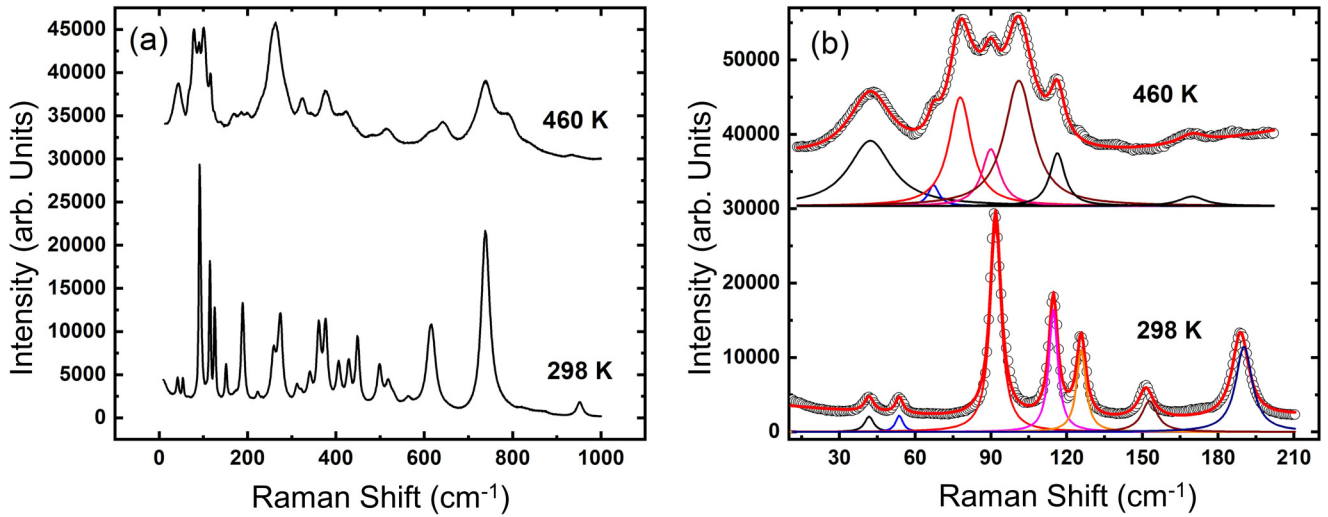
FIG. 9. (a) Raman spectra of Sample B in the frequency range 10–1000 cm^{-1}, as measured at 298 K (monoclinic phase) and 460 K [$Cmc2_1$ (IC) phase]. The large number of almost equal spaced Raman lines with frequencies in the range 100–500 cm^{-1} in the spectrum of the low temperature $P2_1/c$ phase (at 298 K) suggests that the this monoclinic phase involves at least a 4× multiplication of the primitive unit cell of the already modulated orthorhombic $Cmc2_1$ (IC) phase. (b) Low frequency Raman spectra deconvoluted to sum of Lorentzian peaks for monoclinic phase (298 K) and orthorhombic phase (460 K). Individual fitted peaks are also shown.

The temperature dependences of the phonon frequencies are shown in Fig. 8(b). Phonons in the $Cmc2_1$ (IC) phase have stronger dependence on temperature, indicating higher anharmonicity of this phase. The soft mode with frequency 44 cm^{-1} at 443 K originates from the fluctuation in incommensurate structural modulation and would freeze ($\omega = 0$) on transformation to the commensurate phase.

Raman spectral activity (selection rules) is closely related to the point group of the crystal involved. As both the high temperature phases (IC and C) have the same point group, C$_{2v}$, all the zone center ($q = 0$) Raman active phonons of the $Cmc2_1$ (IC) phase are expected to also be active in the $Cmc2_1$ (C) phase. The fact that the soft phonon is frozen in the IC phase and becomes inactive in the C phase suggests that it is a zone boundary (q) phonon of the high temperature $Cmc2_1$ (C) phase. The structural modulation (incommensuration) is driven by this soft zone boundary phonon of $Cmc2_1$ (C) phase, which is observed as a zone center phonon in the $Cmc2_1$ (IC) due to folding of zone boundary phonons into the Brillouin zone center ($q = 0$). A soft zone boundary phonon with frequency 40 cm^{-1} at low temperatures is important in the IC-C phase transition of the isostructural BaMnF$_4$ compound [7].

The Raman spectra measured in low temperature (298 K) monoclinic (point group: C$_{2h}$) and high temperature (460 K) orthorhombic IC phases (point group: C$_{2v}$) are depicted in Fig. 9. Several discernible and unique Raman peaks of the Raman spectrum for the orthorhombic $Cmc2_1$ phase such as those located at 78, 101, 643, 843 cm^{-1} are not observed in the spectrum measured at 298 K, suggesting that absence of any substantial coexistence of orthorhombic $Cmc2_1$ phase at room temperature. The optical phonons in the high temperature orthorhombic phase ($Cmc2_1$) are $\Gamma_{opt} = 11A_1 + 6A_2 + 5B_1 + 11B_2$, where A$_1$, A$_2$, B$_1$ and B$_2$ are nondegenerate Raman active modes, and A$_1$, B$_1$ and B$_2$ are nondegenerate IR active modes [12]. Hence, 33 Raman active nondegenerate optical phonons are expected. On the other hand, the optical

phonons in the room temperature monoclinic phase ($P2_1/c$) are $\Gamma_{opt} = 18A_g + 18B_g + 17A_u + 16B_u$, where A$_g$ and B$_g$ modes are Raman active, and A$_u$ and B$_u$ are IR active [12]. All these A$_g$, B$_g$, A$_u$, B$_u$ modes are nondegenerate. Hence, 36 Raman active nondegenerate optical phonons are expected. Figure 9 shows the Raman spectra of LaTaO$_4$ measured at 298 and 460 K. At 298 K, a total of 26 distinct Raman bands were identified in the frequency range 10–1000 cm^{-1}. On the other hand, at 460 K, only 21 distinct Raman bands could be found in the same frequency range. The number of bands experimentally observed is lower than actually group theoretically predicted ones, which could be due to either accidental degeneracy of band frequency or inadequate intensity arising from small polarizability of several Raman bands [28]. The sharpening of the line widths at low temperature (298 K) is understood to be due to thermal effects. However, the sharpening of the linewidths cannot explain the additional Raman bands observed at low temperature. Raman spectra of the sample were measured in the frequency range 10–1000 cm^{-1} employing a triple monochromator based HORIBA Jobin Yvon micro-Raman spectrometer with a spectral resolution of ~1 cm^{-1}. Therefore, it is clear that the broad Raman bands at 460 K cannot hide peaks spaced more than 1 cm^{-1}. The smallest spacing between the bands in the 298 K spectrum is ~10 cm^{-1} (e.g., there are bands at ~42, 54, 115, and 126 cm^{-1}) as seen in Fig. 9(b). So, they will be well resolved in the 460 K spectrum if at all they were present. Since they are not present in the orthorhombic 460 K spectrum, they do not show up. Thus, those bands are not hidden under the broad bands due to resolution problems. The asymmetric in the line shape in the 460 K spectrum is most likely due to phonon-phonon interaction between same symmetry phonons.

Raman spectroscopy is often useful to infer longer unit cell (Brillouin zone folding) of phase involved in a crystallographic phase transition. If a vibrational branch (such as

a longitudinal optical vibration) is subject to *n* folds of its Brillouin zone, it will give rise to *n*-1 new evenly spaced vibrations of comparable intensity [7,29]. Suppose the unit cell approximately doubles along *c* axis at low temperature T. This will permit Raman spectra of one extra very low frequency optical phonon, which would be described as the Brillouin zone boundary in the high-T phase. Suppose instead that the unit cell quadruples. This will permit three extra lines, almost evenly spaced in frequency. This is the logic behind the argument which suggests that the monoclinic phase of LaTaO$_4$ below $T_{m-o} \sim 443$ K is likely to have at least quadruple multiplication of a primitive unit cell of the high temperature orthorhombic phase. Figure 7 shows that a soft Raman band appears around 44 cm^{-1} in the incommensurate orthorhombic phase near 443 K and disappears in the high temperature orthorhombic C phase above 528 K. Below the orthorhombic IC phase near 443 K, this soft band disappears and a doublet around 42 and 54 cm^{-1} is found. The doublet is worthy of note, because no Raman active phonons are doubly degenerate in any orthorhombic symmetry. Therefore, the peak doubling is more likely to arise from a folding of at least 4× in the unit cell along a particular axis; that is, these two lines are probably low frequency optical modes at $q^*/2$ and $q^*/4$ in the original pseudo-orthorhombic phase, and their doubling is not from the monoclinic distortion but from the unit cell multiplication.

Further support for a large supercell of the monoclinic phase below $T_{m-o} \sim 443$ K comes from the very large number of Raman lines, and from the almost uniform spaced array of nearly half a dozen Raman lines of comparable intensity at 100–500 cm^{-1} in 298 K spectrum (Fig. 9), indicating that vibrational optical branch is subjected to multifold to its Brillouin zone. It can be mentioned that 500 cm^{-1} is a reasonable value for a longitudinal optic phonon (maximum frequency) in a relatively hard material.

IV. DISCUSSION

Results for the $Cmc2_1$(C) → $Cmc2_1$(IC) transition in Sample A appear to be classical with respect to strain and elasticity. The transition temperature from strain data is between 473 and 523 K (Fig. 3), the minimum in shear modulus occurs at ∼510 K and a drop in acoustic attenuation occurs at ∼480 K (Fig. 5). These changes correlate more or less with a peak in permittivity observed at ∼488 K during heating and at ∼483 K cooling (Fig. 2). Incommensurate transitions tend to be second order in character (positive values of coefficient of the Landau fourth order term) but the strain and elasticity data provide direct evidence for significant coupling of the driving order parameter with nonsymmetry breaking strains. This is a classic mechanism for renormalizing the Landau fourth-order coefficient and could be responsible for making it negative, hence accounting for the observed weakly first-order character. The pattern of softening of the shear modulus is similar to the change in velocities of some of the shear modes obtained through the equivalent transition in BaMnF$_4$, as observed by ultrasonic velocity measurements at frequencies of 4–30 MHz [30]. The transition in BaMnF$_4$ (at 250 K) has been described as ferro- to antiferroelectric (FE-AFE) by Scott, where the antiferroelectric (AFE) phase is the orthorhombic phase with

an incommensurate modulation in *c* ($Cmc2_1$ setting) [31], in contrast to the incommensurate modulation in *a* for LaTaO$_4$ [14].

Comparisons of the lattice parameter data for Sample B with those for Sample A indicate a closely similar pattern of strains and first-order character for the $Cmc2_1$(C) → $Cmc2_1$(IC) transition in Sample B. The transition temperature, between 483 and 513 K, is also essentially the same. However, not everything is the same between the two samples. For example, the temperature interval of steep softening ahead of the transition extends up to at least 1140 K in Sample B (Fig. 7) instead of only up to ∼600 K (Fig. 5), but this could be a reflection of the quality of the ceramic in terms of how well-sintered individual grains are to each other. There is also a difference between the evolution of relative permittivity between the two samples (Fig. 2). The peak for Sample A at ∼460–480 K becomes a break in slope at ∼500 K for Sample B. In this context it is worth noting that the dielectric data of Abreu *et al.* [12] for a monoclinic sample, analogous with Sample B, show a frequency dependent peak in permittivity near 500 K which falls ∼5 K below the anomalies in heat capacity (∼510 K) that mark the actual transition point. The increase in permittivity above the transition point shown by Sample B may therefore also be an effect arising from differences in microstructure. More significantly, strong acoustic attenuation below ∼440 K for Sample B must surely be due to the motion of ferroelastic twin walls in monoclinic crystals and the overall softening by ∼80%, instead of ∼20%, must be a reflection of the substantial shear strain ($e_6 \sim 0.06$), which distinguishes the monoclinic structure from the orthorhombic structure.

The patterns of dielectric loss, expressed either as ε" or tanδ, are closely similar for Samples A and B and for other comparable samples reported in the literature [11,12]. The loss is low at room temperatures but increases steeply above ∼400 K with some dependence on frequency [12] or structure type (this study). The pattern of acoustic loss is not exactly the same but Q^{-1} shows a stepwise increase above ∼480 K in the RUS data from Sample A (Fig. 5). Thus, it appears that there is a dielectric loss mechanism that emerges at the same temperature and measuring frequencies as a change in acoustic attenuation in Sample A. A classic acoustic loss mechanism involves motion under stress of crack tips or grain boundaries but the association with the phase transition of Sample A rules this out. There is also elastic softening in a temperature interval of ∼100 K ahead of the transition, which is a typical indicator of precursor fluctuations. The most obvious explanation for the samples examined here is that the crystals contain local regions that have dynamical variations of both strain and polarity with relaxation times of ∼10^{-5}–10^{-6} s. It is not possible to be more specific without other experimental evidence, such as from inelastic neutron scattering, but other examples of ferroelectric materials with significant acoustic loss attributed to dynamical clusters have been reviewed by Carpenter [25].

The IC-C transition is driven by a soft zone-boundary phonon of the commensurate orthorhombic phase that becomes a zone center mode of the IC structure, with its frequency increasing from ∼30 cm^{-1} at the transition point T_{IC-C} to ∼45 cm^{-1} at 443 K. From observation of the low

frequency doublet (42 and 54 cm^{-1}), and several equally spaced spectral lines between 100 and 500 cm^{-1} in the monoclinic phase compared to the high temperature incommensurate orthorhombic phase, it is proposed that the monoclinic phase also contains a superstructure. The extra spectral lines are more likely to arise from at least a 4× multiplication of the primitive unit cell along a particular axis, and their splitting is not from the monoclinic distortion (there are no degeneracies involved in the phonon mode vibrations to split in the low-temperature monoclinic phase transition). The possibility of an incommensurately modulated structure in the monoclinic phase requires additional study.

V. CONCLUSION

Following the recent discovery of an intermediate incommensurate (IC) orthorhombic [$Cmc2_1(\alpha00)0s0$] phase [14], PND, RUS, and Raman spectroscopy have been used to examine the structural evolution of LaTaO$_4$ in terms of symmetry, strain, elasticity, and phonon behavior. They have been combined to examine the first-order transitions between the monoclinic $P2_1/c$ and IC orthorhombic $Cmc2_1(\alpha00)0s0$ phases and IC-C $Cmc2_1$ transition. We show that the IC-C transition that occurs between 500 and 530 K, is strikingly similar to that observed in the $n = 2$ fluoride, BaMnF$_4$, despite the IC modulation being more akin to that found in the $n = 4$ oxides. Low frequency Raman spectroscopic studies

support the idea that the IC-C transition is driven by a soft zone-boundary phonon, i.e., giving a superstructure below $T_{\text{IC}-\text{C}}$, but interestingly, this study also suggests that the monoclinic phase could possess a superstructure of at least four times that of the primitive orthorhombic unit cell. Hence, the $P2_1/c \rightarrow Cmc2_1$ transition, which exhibits classic first-order behavior, may be between two modulated phases.

[1] M. Núñez Valdez and N. A. Spaldin, Origin and evolution of ferroelectricity in the layered rare-earth-titanate, R$_2$Ti$_2$O$_7$, Carpy-Galy phases, Polyhedron **171**, 181 (2019).

[2] A. Carpy, P. Amestoy, and J. Galy, Contribution à l'étude du pyroniobate de calcium Ca$_2$Nb$_2$O$_7$, C. R. Acad. Sci. Paris C **275**, 833 (1972).

[3] P. Daniels, R. Tamazyan, C. A. Kuntscher, M. Dressel, F. Lichtenberg, and S. van Smaalen, The incommensurate modulation of the structure of Sr$_2$Nb$_2$O$_7$, Acta Crystallogr. Sect. B **58**, 970 (2002).

[4] N. Ishizawa, K. Ninomiya, and J. Wang, Structural evolution of La$_2$Ti$_2$O$_7$ at elevated temperatures, Acta Crystallogr. Sect. B **75**, 257 (2019).

[5] M. Eibschütz, H. J. Guggenheim, S. H. Wemple, I. Camlibel, and M. DiDomenico, Ferroelectricity in BaM^{2+}F$_4$, Phys. Lett. A **29**, 409 (1969).

[6] K. Shimamura, E. G. Víllora, H. Zeng, M. Nakamura, S. Takekawa, and K. Kitamura, Ferroelectric properties and poling of BaMgF$_4$ for ultraviolet all solid-state lasers, Appl. Phys. Lett. **89**, 232911 (2006).

[7] J. F. Ryan and J. F. Scott, Raman study of soft zone-boundary phonons and antiferrodistortive phase transition in BaMnF$_4$, Solid State Commun. **14**, 5 (1974).

[8] K. P. F. Siqueira and A. Dias, Effect of the processing prameters on the crystalline structure of lanthanide orthotantalates, Mater. Res. **17**, 167 (2014).

[9] F. Vullum, F. Nitsche, S. M. Selbach, and T. Grande, Solid solubility and phase transitions in the system LaNb$_{1-x}$Ta$_x$O$_4$, J. Solid State Chem. **181**, 2580 (2008).

[10] R. J. Cava and R. S. Roth, The structure analysis of LaTaO$_4$ at 300 °C by neutron powder profile analysis, J. Solid State Chem. **36**, 139 (1981).

[11] K. J. Cordrey, M. Stanczyk, C. A. L. Dixon, K. S. Knight, J. Gardner, F. D. Morrison, and P. Lightfoot, Structural and dielectric studies of the phase behavior of the topological ferroelectric La$_{1-x}$Nd$_x$TaO$_4$, Dalton Trans. **44**, 10673 (2015).

[12] Y. G. Abreu, K. P. F. Siqueira, F. M. Matinaga, R. L. Moreira, and A. Dias, High-temperature antiferroelectric and ferroelectric phase transitions in phase pure LaTaO$_4$, Ceram. Int. **43**, 1543 (2017).

[13] X. Q. Liu, G. J. Li, and X. M. Chen, Topological ferroelectricity in layered perovskite LaTaO$_4$: A first principles study, Solid State Commun. **247**, 31 (2016).

[14] G. W. Howieson, S. Wu, A. S. Gibbs, W. Zhou, J. F. Scott, and F. D. Morrison, Incommensurate-commensurate transition in the geometric ferroelectric LaTaO$_4$, Adv. Funct. Mater. **30**, 2004667 (2020).

[15] A. C. Larson and R. B. Von Dreele, General structure analysis system (GSAS), Los Alamos National Laboratory Report LAUR 86-748 (1994).

[16] B. H. Toby, EXPGUI, a graphical user interface for GSAS, J. Appl. Crystallogr. **34**, 210 (2001).

[17] V. Petříček, M. Dušek, and L. Palatinus, Crystallographic computing system JANA2006: General features, Z. Krist. - Cryst. Mater. **229**, 345 (2014).

[18] See Supplemental Material at http://link.aps.org/supplemental/10.1103/PhysRevB.103.014119 for details of the refinement of powder neutron diffraction data, refinement profiles and summary of structural information; details of RUS data collection.

[19] A. Migliori and J. L. Sarrao, *Resonant Ultrasound Spectroscopy: Applications to Physics, Materials Measurements, and Nondestructive Evaluation* (Wiley, New York, 1997).

[20] R. E. A. McKnight, T. Moxon, A. Buckley, P. A. Taylor, T. W. Darling, and M. A. Carpenter, Grain size dependence of elastic anomalies accompanying the α-β phase transition in polycrystalline quartz, J. Phys.: Condens. Matter **20**, 075229 (2008).

[21] C. Ablitt, S. Craddock, M. S. Senn, A. A. Mostofi, and N. C. Bristowe, The origin of uniaxial negative thermal expansion in layered perovskites, Npj Comput. Mater. **3**, 44 (2017).

[22] M. A. Carpenter, A. I. Bacerro, and F. Seiferi, Strain analysis of phase transitions in (Ca, Sr)TiO$_3$ perovskites, Am. Mineral. **86**, 348 (2001).

[23] M. A. Carpenter, E. K. H. Salje, and A. Graeme-Barber, Spontaneous strain as a determinant of thermodynamic properties for phase transitions in minerals, Eur. J. Mineral. **10**, 621 (1998).

[24] M. A. Carpenter, E. K. H. Salje, A. Graeme-Barber, B. Wruck, M. T. Dove, and K. S. Knight, Calibration of excess thermodynamic properties and elastic constant variations associated with the $\alpha \leftrightarrow \beta$ phase transition in quartz, Am. Mineral. **83**, 2 (1998).

[25] M. A. Carpenter, Static and dynamic strain coupling behavior of ferroic and multiferroic perovskites from resonant ultrasound spectroscopy, J. Phys.: Condens. Matter **27**, 263201 (2015).

[26] M. Quilichini, J. F. Ryan, J. F. Scott, and H. J. Guggenheim, Light scattering from soft modes in ferroelectric BaZnF$_4$ and BaMgF$_4$, Solid State Commun. **16**, 471 (1975).

[27] T. R. Ravindran, V. Sivasubramanian, and A. K. Arora, Low temperature Raman spectroscopic study of scandium molybdate, J. Phys. Condens. Matter **17**, 277 (2005).

[28] K. K. Mishra, S. Chandra, N. P. Salke, S. N. Achary, A. K. Tyagi, and R. Rao, Soft modes and anharmonicity in H$_3$[Co(CN)$_6$]: Raman spectroscopy and first-principles calculations, Phys. Rev. B **92**, 134112 (2015).

[29] W. Dultz, H. Krause, and L. W. Winchester, The Raman spectrum of NaCN under hydrostatic pressure, J. Chem. Phys. **67**, 2560 (1977).

[30] I. J. Fritz, Ultrasonic velocity measurements near the 250 °K phase transition in BaMnF$_4$, Phys. Lett. A **51**, 219 (1975).

[31] J. F. Scott, Phase transitions in BaMnF$_4$, Rep. Prog. Phys. **42**, 1055 (1979).

[32] https://doi.org/10.5286/ISIS.E.RB1820307